

Article

# Atmospheric and Radiometric Correction Algorithms for the Multitemporal Assessment of Grasslands Productivity

Jesús A. Prieto-Ampan <sup>1</sup>, Federico Villarreal-Guerrero <sup>1</sup>, Martin Martinez-Salvador <sup>1</sup>, Carlos Manjarrez-Domínguez <sup>2</sup>, Eduardo Santellano-Estrada <sup>1</sup> and Alfredo Pinedo-Alvarez <sup>1,\*</sup>

<sup>1</sup> Facultad de Zootecnia y Ecología, Universidad Autónoma de Chihuahua, Periférico Francisco R. Almada Km 1, Chihuahua, Chihuahua 31453, Mexico; jesus\_prieto06@hotmail.com (J.A.P.-A.); fvillarreal@uach.mx (F.V.-G.); masm750130@gmail.com (M.M.-S.); esantellano@uach.mx (E.S.-E.)

<sup>2</sup> Facultad de Ciencias Agrotecnológicas, Universidad Autónoma de Chihuahua, Chihuahua 31350, Mexico; manjarrez.carlos@gmail.com

\* Correspondence: apinedo@uach.mx; Tel.: +52-(614)-434-0363; Fax: +52-(614)-434-0345

Received: 7 November 2017; Accepted: 26 January 2018; Published: 1 February 2018

**Abstract:** A key step in the processing of satellite imagery is the radiometric correction of images to account for reflectance that water vapor, atmospheric dust, and other atmospheric elements add to the images, causing imprecisions in variables of interest estimated at the earth's surface level. That issue is important when performing spatiotemporal analyses to determine ecosystems' productivity. In this study, three correction methods were applied to satellite images for the period 2010–2014. These methods were Atmospheric Correction for Flat Terrain 2 (ATCOR2), Fast Line-of-Sight Atmospheric Analysis of Spectral Hypercubes (FLAASH), and Dark Object Subtract 1 (DOS1). The images included 12 sub-scenes from the Landsat Thematic Mapper (TM) and the Operational Land Imager (OLI) sensors. The images corresponded to three Permanent Monitoring Sites (PMS) of grasslands, 'Teseachi', 'Eden', and 'El Sitio', located in the state of Chihuahua, Mexico. After the corrections were applied to the images, they were evaluated in terms of their precision for biomass estimation. For that, biomass production was measured during the study period at the three PMS to calibrate production models developed with simple and multiple linear regression (SLR and MLR) techniques. When the estimations were made with MLR, DOS1 obtained an  $R^2$  of 0.97 ( $p < 0.05$ ) for 2012 and values greater than 0.70 ( $p < 0.05$ ) during 2013–2014. The rest of the algorithms did not show significant results and DOS1, which is the simplest algorithm, resulted in the best biomass estimator. Thus, in the multitemporal analysis of grassland based on spectral information, it is not necessary to apply complex correction procedures. The maps of biomass production, elaborated from images corrected with DOS1, can be used as a reference point for the assessment of the grassland condition, as well as to determine the grazing capacity and thus the potential animal production in such ecosystems.

**Keywords:** Landsat; ATCOR2; DOS1; FLAASH; spatio temporal

## 1. Introduction

Grassland ecosystems play an important role in biodiversity conservation, ecosystem services provision, and the global carbon cycle [1]. They also play a key role in biogeochemical cycles and the exchange of energy [2]. However, grasslands have experienced a notorious degradation in recent years due to long droughts, climate variability, fragmentation and anthropic intervention. The application of improper management practices has been one of the main causes of such degradation [3,4]. Specifically, grasslands in northern Mexico are extensively used for cattle grazing and have also experienced intensive land-use change due to agricultural activities, which has resulted in changes of the species composition on such ecosystems [4,5].

Accurate monitoring and evaluation of grasslands' conditions is critical for their conservation and, in some cases, their restoration [6]. In the past decades, biomass inventory of grasslands has been driven by traditional methods of evaluation, which include extensive field sampling [7,8]. Even though these methods are accurate, they are costly, as well as time- and labor-consuming, when large pieces of land have to be covered [9]. With the aim of developing more effective monitoring methods, there have been numerous studies on indirect methods to estimate the biomass of grasslands using remote sensing information [10–12]. In this endeavor, optical sensors, radar, and Lidar systems have been used [13]. In general, all these studies have sought to find relationships between grassland structural variables and satellite image spectral data [14].

For instance, Marsett et al. [15] used image-processing algorithms to quantify the total cover, height, and biomass of grasslands. Comparisons of remote sensor estimates with independent field measurements yielded values of  $R^2 = 0.80, 0.85, \text{ and } 0.77$  and Nash Sutcliffe coefficient values of 0.78, 0.70, and 0.77 for coverage, plant height, and biomass, respectively. Dusseux et al. [16] correlated spectral data from the Satellite Pour l'Observation de la Terre (SPOT) sensor converted to indices, such as the leaf area index, the Normalized Difference Vegetation Index, and the vegetation cover fraction, with data of biomass measured in the field. The coefficients of determination found were  $R^2 = 0.68, 0.30, \text{ and } 0.50$ . These studies demonstrated the good relationships between the spectral information from the remote sensors and the biomass inventories in the field. Rodríguez-Maturino et al. [17] correlated 3-year data from Landsat TM5 as well as field measurements of coverage of grass canopy and grass height, obtaining values of  $R^2$  greater than 0.70.

The Landsat satellite has provided data since 1972 [18] with an extensive global coverage. This is an important resource for monitoring global environmental change [19–21]. However, the problem of saturation of data in the images is considered an important factor affecting the results when estimating the biomass of vegetation [22–24]. This phenomenon of saturation is caused by atmospheric dispersion and absorption, which has substantial variations with time, space, and wavelength. In addition, the surface reflectance is strongly affected by the elevation of the terrain, a more evident effect in mountainous environments [25]. All of these factors determine the importance of atmospheric correction to attenuate the effects of noise occurring in the capture of satellite images [26,27], especially when multitemporal studies are carried out [28–30].

Different atmospheric and radiometric correction methods have been developed to transform the original values of the images into values of reflectance [31–33]. Several of these techniques have been developed to estimate the amount of atmospheric bias from thin-surface terrestrial images by assessing the molecular and aerosol dispersion [34,35]. For instance, the algorithm called Fast Line of sight Atmospheric Analysis of Spectral Hypercubes (FLAASH) serves to derive surface and atmospheric reflectance properties using a MODTRAN accuracy model developed by Spectral Science Inc. (Burlington, MA, USA) [36], which explains the effects of adjacency associated with the dispersion of the atmosphere. The method of Atmospheric Correction for Flat Terrain 2 (ATCOR2) removes the brightness of the image, as well as the possible effects of fog or clouds, to obtain the values of the terrestrial surface [37,38]. The method of Dark Object Subtract 1 (DOS1) is based on the properties of the image and is the algorithm most widely used for the detection of land-use changes [39,40].

There have been some studies on the comparison of different approaches to correct the atmospheric effects. In this regard, El Hajj et al. [41] compared relative radiometric normalization and a 6S algorithm employing SPOT5 data. Chang et al. [42] evaluated the correction methods TOA, GDOS, and AC performed on Landsat images. Calliceco and Dell'Acqua [43] compared the algorithms 6S and MODTRAN. Agrawal et al. [44] compared the FLAASH and QUAC algorithms. Nazer et al. [45] compared five atmospheric correction algorithms, 6S, FLAASH, ATCOR, DOS, and ELM, over sand, turf, grass, and water surfaces. López-Serrano et al. [46] evaluated the performance of the COST, ATCOR2, FLAASH, 6S, and TOA algorithms for the estimation of forest above-ground biomass. Martins et al. [47] compared the 6S, ACOLITE, and Sen2Cor methods applied to the new platform Sentinel 2-MSI. However, these studies lack the multitemporal component and

only a few studies [48–50] have been developed to compare the methods of radiometric correction on different dates.

Based on the aforementioned, most of the studies are not multitemporal; they neither compare correction methods at different dates nor determine the grasslands biomass productivity in semi-arid regions. The objective of this study was to compare three correction methods based on their precision for the estimation of grassland biomass on the semi-arid ecosystems of Chihuahua, Mexico. Two atmospheric (ATCOR2, FLAASH) correction methods and one radiometric (DOS1) correction method were evaluated. The results may serve grassland owners for decision-making on animal load adjustments. Likewise, government institutions and non-governmental organizations working in areas such as forestry, agriculture, livestock research, and rural development could use this information for planning, decision-making, and the development of public policies.

## 2. Materials and Methods

### 2.1. Study Area

The study included three Permanent Monitoring Sites (PMS), which belong to the National Livestock Oriented Land Monitoring System [51]. The first PMS is called 'Teseachi', located at the central coordinates 28°53'35"N, 107°26'49"W; the second PMS, called 'El Sitio', is located at 27°35'17"N, 106°16'30"W; the third PMS, called 'Eden', is located at 27°06'50"N and 105°26'46"W (Figure 1). Each PMS is composed of nine monitoring stations, where biomass sampling was carried out once a year. The three PMS are located in the semi-arid region of Chihuahua, where the vegetation is dominated by grasses. Besides the grasslands, this region also houses chaparral vegetation and dunes [52]. Grasslands provide habitat for wildlife, serve as reservoirs of carbon, and help mitigate global environmental change impacts [53]. In these ecosystems, it is possible to find mammals, such as *Bison bison* and *Cynomys ludovicianus*, which have multiple effects on grasslands, and both of them are considered key in maintaining grassland habitats [54]. In addition, mammals such as *Puma concolor* can also be found, which is in a decreasing status based on the International Union for Conservation of Nature (IUCN) red list [55].

### 2.2. Biomass Sampling

The data on biomass employed for this study comes from values registered on the field during the period 2010–2014. During the first year of sampling, the sites were plenty identified. The center site and the corner boundaries were marked with flags. These points got recorded with a global positioning system (GPS) to ensure that the biomass sampling was performed at the same locations during all of the years studied. The biomass was sampled during the month of October. During this period, the maximum peak of biomass is achieved and the vegetation offers a strong reflectance [56].

The sampling design for the biomass collection in each PMS was based on the shape and size of a pixel of a satellite image. The PMS is a quadrangular area of 225 ha (1.5 km × 1.5 km). In its interior, the PMS includes nine sampling stations of 1.0 ha each (100 m × 100 m). The centers of the sampling stations were located 200 m apart. The sampling stations consisted of a cross, which was marked from North to South and East to West. The cross served to locate its four corresponding quadrants. Within each quadrant, a circled area of 1.6 m of diameter was randomly marked. The circles were built with heat-resistant, orange color, plastic tubes of 0.02 m diameter, which are commonly employed for electrical wire protection. The biomass inside the quadrants was cut with sizers and placed in paper bags. The bags were tagged to clearly identify the sites where the biomass came from. The bags were then oven dried for 48 h at 70 °C and the database was built with the values of these dry weights (kg·ha<sup>-1</sup>).

A detailed description of the field sampling design and data collection protocol can be found in [51].

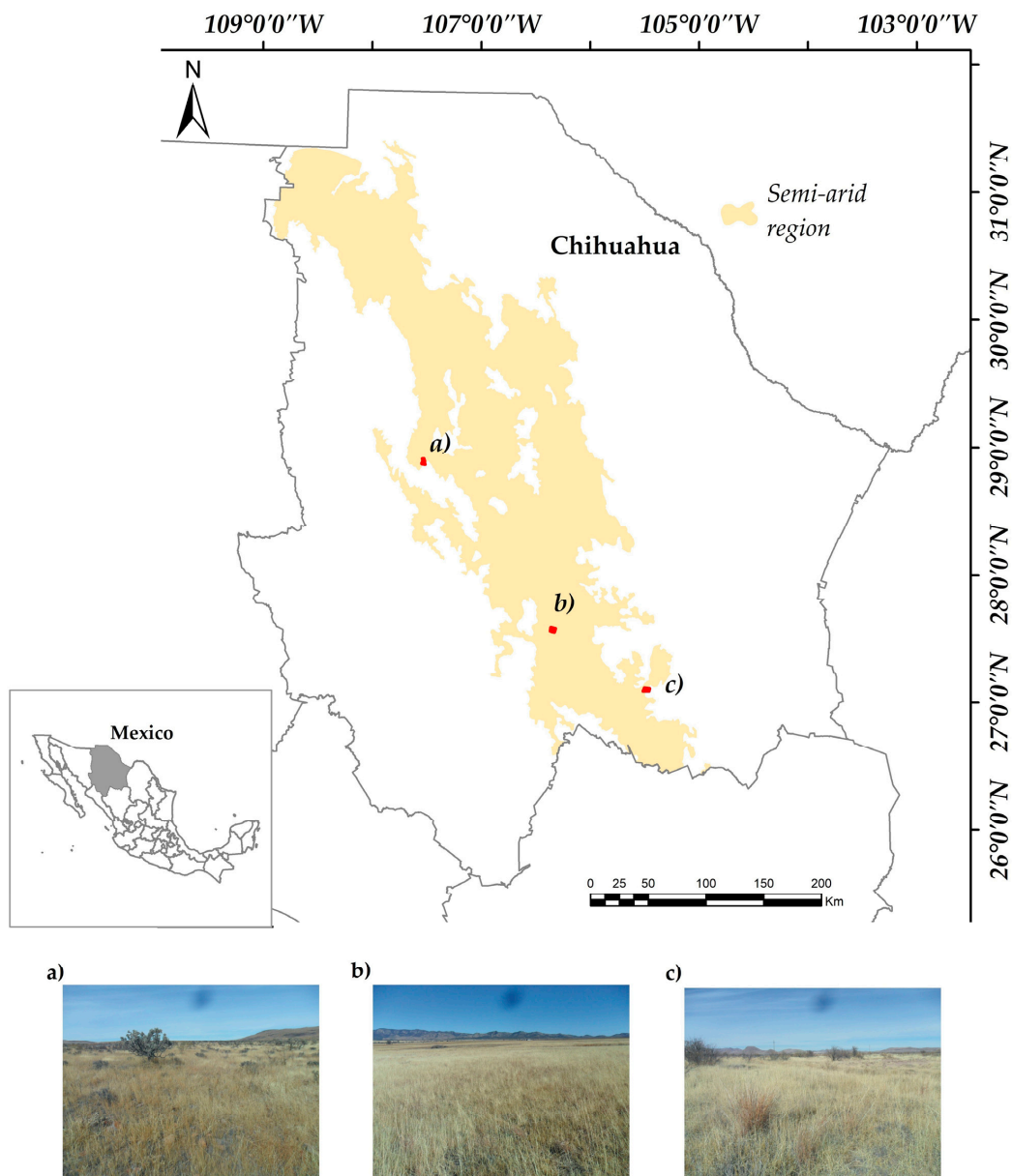


**Figure 1.** Location of the three permanent monitoring sites. The pictures depict representative biomass features of the sites. (a) Teseachi; (b) El Sitio; (c) Eden.

### 2.3. Satellite Data

A total of 12 images, including scenes taken by the Landsat Thematic Mapper (TM) and the Operational Land Imager (OLI), available at the United States Geological Survey [57], were used. The scenes had a spatial resolution of  $30\text{ m} \times 30\text{ m}$  and correspond to the period of 2010–2014 (Table 1). The sensors operate with several bands filtered from the electromagnetic spectrum. The Landsat TM is equipped with band 1 ( $0.45\text{--}0.52\ \mu\text{m}$ ), band 2 ( $0.52\text{--}0.60\ \mu\text{m}$ ), band 3 ( $0.63\text{--}0.69\ \mu\text{m}$ ), band 4 ( $0.76\text{--}0.90\ \mu\text{m}$ ), band 5 ( $1.55\text{--}1.75\ \mu\text{m}$ ), and band 7 ( $2.08\text{--}2.35\ \mu\text{m}$ ). Likewise, the OLI is equipped with band 2 ( $0.45\text{--}0.51\ \mu\text{m}$ ), band 3 ( $0.53\text{--}0.59\ \mu\text{m}$ ), band 4 ( $0.64\text{--}0.67\ \mu\text{m}$ ), band 5 ( $0.85\text{--}0.88\ \mu\text{m}$ ), band 6 ( $1.57\text{--}1.65\ \mu\text{m}$ ), and band 7 ( $2.11\text{--}2.29\ \mu\text{m}$ ) [58].

**Table 1.** Characteristics of Landsat Thematic Mapper (TM) and Operational Land Imager (OLI) scenes used in the study.

PMS	Scene ID	Date of Image	Sensor	Path/Row
Eden	LT50310412010279EDC00	6 October 2010	TM	31/41
	LT50310412011298EDC00	25 October 2011		
	LC80310412013319LGN00	15 November 2013	OLI	
	LC80310412014274LGN00	1 October 2014		
El Sitio	LT50320412010302EDC00	29 October 2010	TM	32/41
	LT50320412011305EDC00	1 November 2011		
	LE70320412012028EDC00	28 October 2012	OLI	
	LC80320412013278LGN00	5 October 2013		
Teseachi	LC80320412014281LGN00	8 October 2014		
	LT50330402010309EDC00	5 November 2010	TM	33/40
	LT50330402011296EDC00	23 October 2011		
	LE70330402012339EDC00	4 December 2012		
	LC80330402013285LGN00	12 October 2013	OLI	
LC80330402014288LGN00	15 October 2014			

#### 2.4. Correction Methods

The correction methods (CM) used to eliminate the noise in the satellite images were: ATCOR2, FLAASH, and DOS1. The ATCOR2 method removes the brightness of the image, as well as the possible effects of fog or clouds, to obtain the values of the terrestrial surface [37]. It also uses predetermined sensor calibration values as well as solar angles to obtain reflectance values [33]. This method is based on the MODerate resolution atmospheric TRANsmission (MODTRAN) radioactive transfer model [59]. The main characteristics of ATCOR2 are: a pre-classification of the scene (soil, water, fog, and clouds), recovery of atmospheric parameters (aerosol optical thickness, water vapor) and surface reflectance recovery [60]. The surface reflectance ( $\rho_{SUP}$ ) is obtained by Equation (1).

$$\rho_{SUP} = \frac{1}{a_1} \left( \frac{d^2 \pi L_{TOA}}{E_{TOA} \cos \theta_i} - a_0 \right) \quad (1)$$

where  $d$  is the direct distance to the sun,  $L_{TOA}$  is the spectral radiance of the satellite,  $E_{TOA}$  is the solar spectral radiance on a surface perpendicular to the rays of the sun outside the atmosphere, and  $\theta_i$  is the solar zenith angle. To obtain the coefficients  $a_0$  and  $a_1$ , the standard atmospheric parameters (aerosol type, visibility or optical thickness, and water vapor column) are required. Such parameters are available in the Software ERDAS© (v.2014). For this study, the solar model used was rural with a scene visibility of 40 km. In addition, the parameter of tropical\_rural was chosen based on the dates the scenes were taken.

The mean reflectance of the studied area  $\bar{\rho}_{SUP_i}$  is calculated to correct for the adjacency effect. Therefore, Equation (2) describes the relation to obtain the reflectance of the free surface of the adjacency effect.

$$\rho'_{SUP} = \rho_{SUP} + \left( \int_{\lambda}^{\lambda_2} \frac{\tau_{0dif}}{\tau_{0dir}} R d\lambda \right) \left( \rho_{SUP} - \sum_{i=1}^{n_R} \bar{\rho}_{SUP_i} w_i \right) \quad (2)$$

where  $\tau_{0dif}$  and  $\tau_{0dir}$  are the diffuse and direct transmittance, respectively,  $R$  is the sensor-specific spectral response curve, and  $w_i$  defines the weighting coefficients as a function of the distance-dependence. The atmospheric correction was carried out with the ATCOR2 module of the software ERDAS© (v.2014).

The FLAASH algorithm is also based on the MODTRAN radiative transfer model [61,62]. It is designed to eliminate the atmospheric effects caused by the molecular dispersion of particles in the atmosphere. It is determined by Equation (3).

$$L_{TOA} = \left( \frac{A\rho_{SUP}}{1 - \rho_e S} \right) \left( \frac{B\rho_e}{1 - \rho_e S} \right) + L_o \quad (3)$$

where  $L_{TOA}$  is the spectral radiance reached by the satellite,  $\rho_{SUP}$  is the reflectance of the pixel surface,  $\rho_e$  is the reflectance of the average surface of the pixel of the surrounding region,  $S$  is the spherical albedo of the atmosphere,  $L_o$  is the radiance backscattered by the atmosphere, and  $A$  as well as  $B$  are coefficients that depend on the atmosphere and geometric conditions.

The first term of the equation corresponds to the reflectance of the surface that travels directly into the sensor while the second term corresponds to the luminosity of the surface that is dispersed by the environment. The distinction between  $\rho_{SUP}$  and  $\rho_e$  explains the “adjacency effect” (spatial blending of radiation between nearby pixels) caused by the atmospheric dispersion. The values of  $A$ ,  $B$ ,  $S$ , and  $L_o$  can be determined empirically from the MODTRAN4 standards. The vision and the solar angles of the measurement and the nominal values for the surface elevation, aerosol shape, and visible range of the scene must be specified [60]. For this study, the standard model used was tropical, which is recommended for locations with Latitudes around  $30^\circ$  when the scenes are taken in September–October. The terrain elevation values used were 1818.13, 1450.5, and 2114.5 meters above the sea level for El Sitio, Eden, and Teseachi, respectively. In addition, the aerosol type was chosen as rural with a scene visibility of 40 km, corresponding to zones with clean weather conditions, as this is the case for the three sites analyzed in this study. This correction method was carried out with the FLAASH module of the software ENVI© (v.5.1).

The DOS1 method is based on the properties of the image. This correction method is the most widely used for the detection of land-use changes. Elements such as water, forests, and shadows are considered as dark objects when their values of reflectance are close to zero. Dark objects are detected automatically when the pixel reflectance value is less than or equal to 1.0%. The assumption is that some pixels within the image receive 0% of the solar radiation (100% of shade), mainly due to the effect of topography, and the value of radiances corresponding to these pixels registered by the satellite correspond to atmospheric dispersion [31]. If a dark object is found in the image, the minimum reflectance value in the histogram is assigned to such an object. From this minimum, it is possible to correct the entire scene by the effects of the atmospheric dispersion [39,40]. To obtain the surface reflectance, Equation (4) is used.

$$\rho_{SUP} = \frac{d^2 \pi (L_{TOA} - L_o)}{E_{TOA} \cos\theta_i} \quad (4)$$

where  $d$  is the direct distance to the sun,  $L_{TOA}$  is the spectral radiance to the satellite,  $L_o$  is the backscatter glow through the atmosphere,  $E_{TOA}$  is the solar spectral radiance on a surface perpendicular to the sun’s rays outside the atmosphere, and  $\theta_i$  is the solar zenith angle. The radiometric correction was carried out with the Semi-Automatic Classification plugin developed by Congedo [63] and included in the software QGIS (v.2.18).

## 2.5. Accuracy of the Correction Methods

A visual analysis of false color compositions was performed to compare the correction methods (CMs). Statistical analyses included an ANOVA and a means comparison of the spectral signatures per band, carried out in the software SAS© (v.9.1.3). In addition, a simple linear regression (SLR) analysis was carried out between the values of each CM, separately per band, and the biomass. Moreover, a multivariate principal component (PC) analysis was performed. The components that explained at least 80% of the total variability of the reflectance values of each CM were selected. The accuracy

of the CMs was determined by SLR when only one main component was selected and by multiple linear regression (MLR) in the cases when two or more components were selected. In any case, the coefficient of determination ( $R^2$ ) and the root mean square error (RMSE) were quantified to find the CM that best fitted the data of each year and each sampling site analyzed. Likewise, the  $p$  value served to determine the reliability of the CMs to estimate the biomass. A flow diagram explaining the methodology followed in this study is represented in Figure 2.

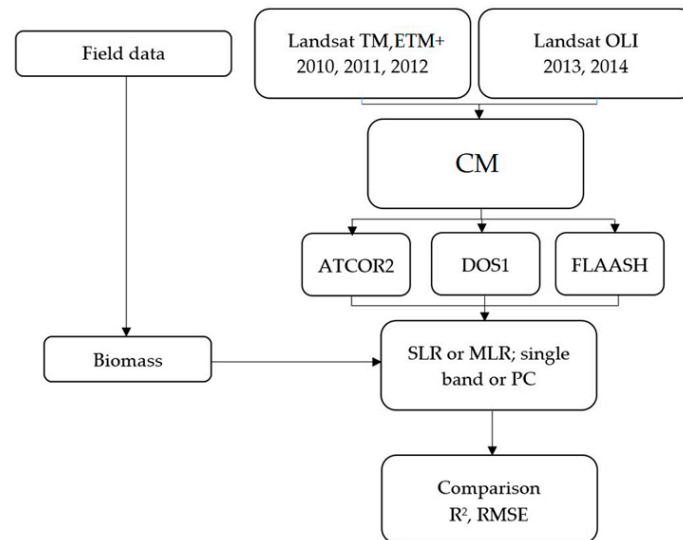


**Figure 2.** Flow diagram representing the procedure followed for the analysis. CM: correction method; SLR: simple linear regression; MLR: multiple linear regression; PC: principal component; RMSE: root mean square error.

### 3. Results

#### 3.1. Composition of Radiometrically Corrected Images

In a first analysis, the radiometrically corrected false-color images for Eden (years 2010, 2011, 2013, and 2014), as well as El Sitio and Teseachi (years 2010, 2011, 2012, 2013, and 2014), as is shown in Figures 3–5, were visually compared. The correction methods were configured using the parameter of rural zone, which is a pre-calibrated value for zones not affected by urban zones or industrial activities [60].

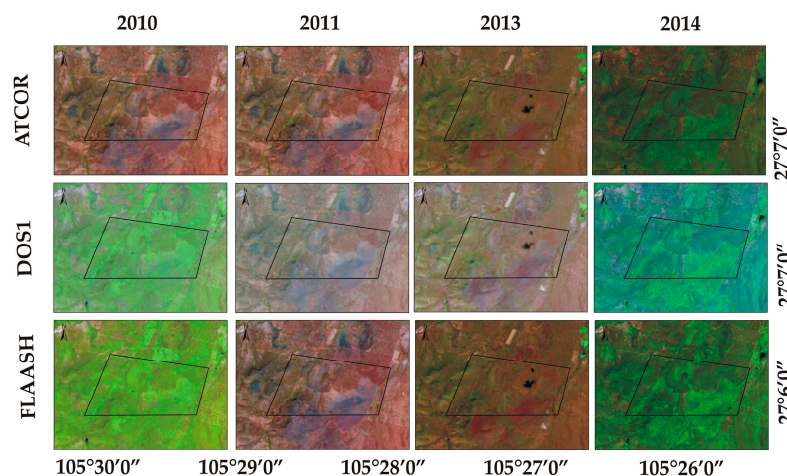


**Figure 3.** False-color images from the different radiometric correction algorithms. Site: Eden.

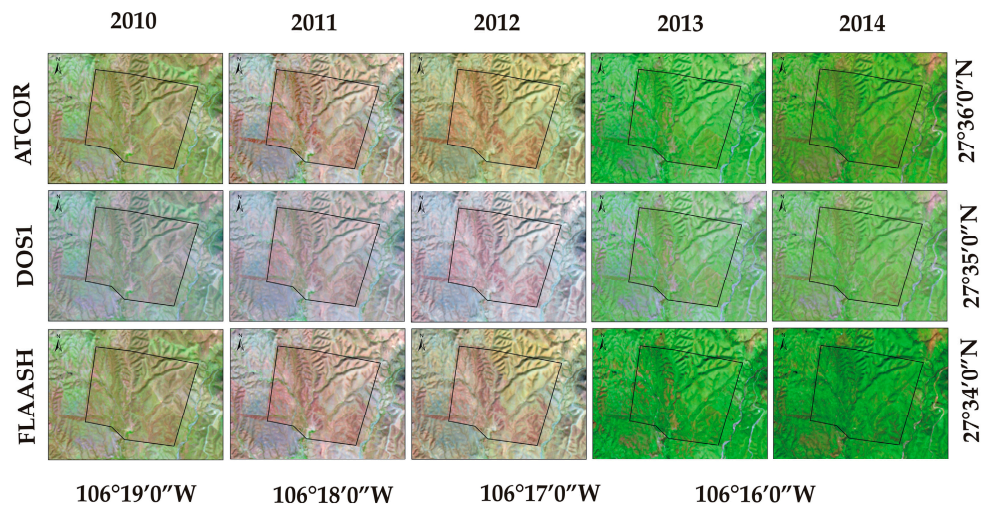


**Figure 4.** False-color images from the different radiometric correction algorithms. Site: El Sitio.

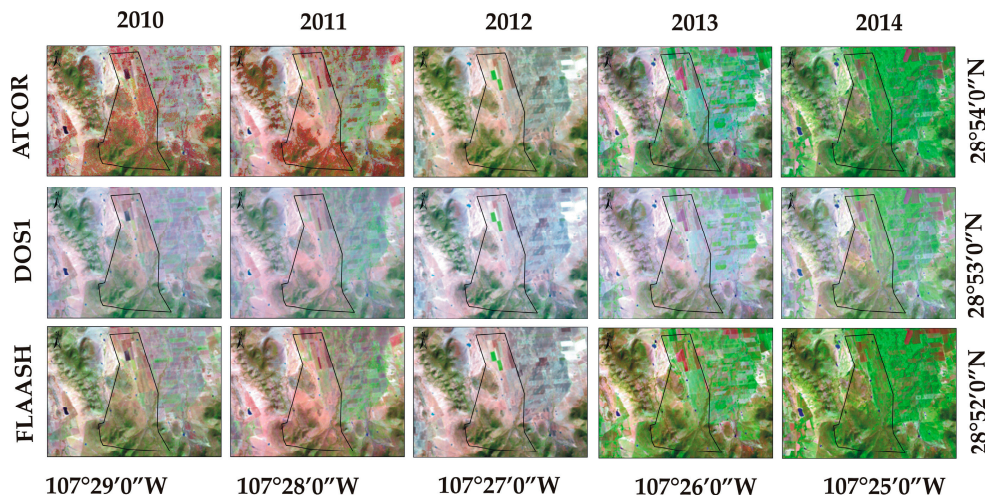


**Figure 5.** False-color images from the different radiometric correction algorithms. Site: Teseachi.

### 3.2. Comparative Analysis of the Correction Methods

The reflectance means from the three PMS, obtained after applying the CMs for the period 2010–2014, were compared (Figures 6–8). The differences among the CMs in general varied. The spectral signature of the grassland showed low reflectance values for the bands blue, green, and red during the studied period. Conversely, high values of reflectance were obtained by the bands corresponding to the Near Infra-Red (NIR) and Shortwave Infra-Red (SWIR) regions for the three PMS. That was possibly due to a strong chlorophyll absorption.

The DOS1 and ATCOR2 methods presented higher values of surface reflectance than the FLAASH method in the visible region for most of the years. This situation may have been induced due to the configuration of DOS1 and ATCOR2, which ignore the effects of atmospheric dispersion on the spectral signatures. In particular, DOS1 does not have the capability to simulate the atmospheric absorption and produces a decrement of surface reflectance [64]. These dissimilarities are also due to some combinations of adjustments in the radiometric calibration [65]. Furthermore, it could also be due to the effects caused by the heterogeneity of the sites and the grassland itself.

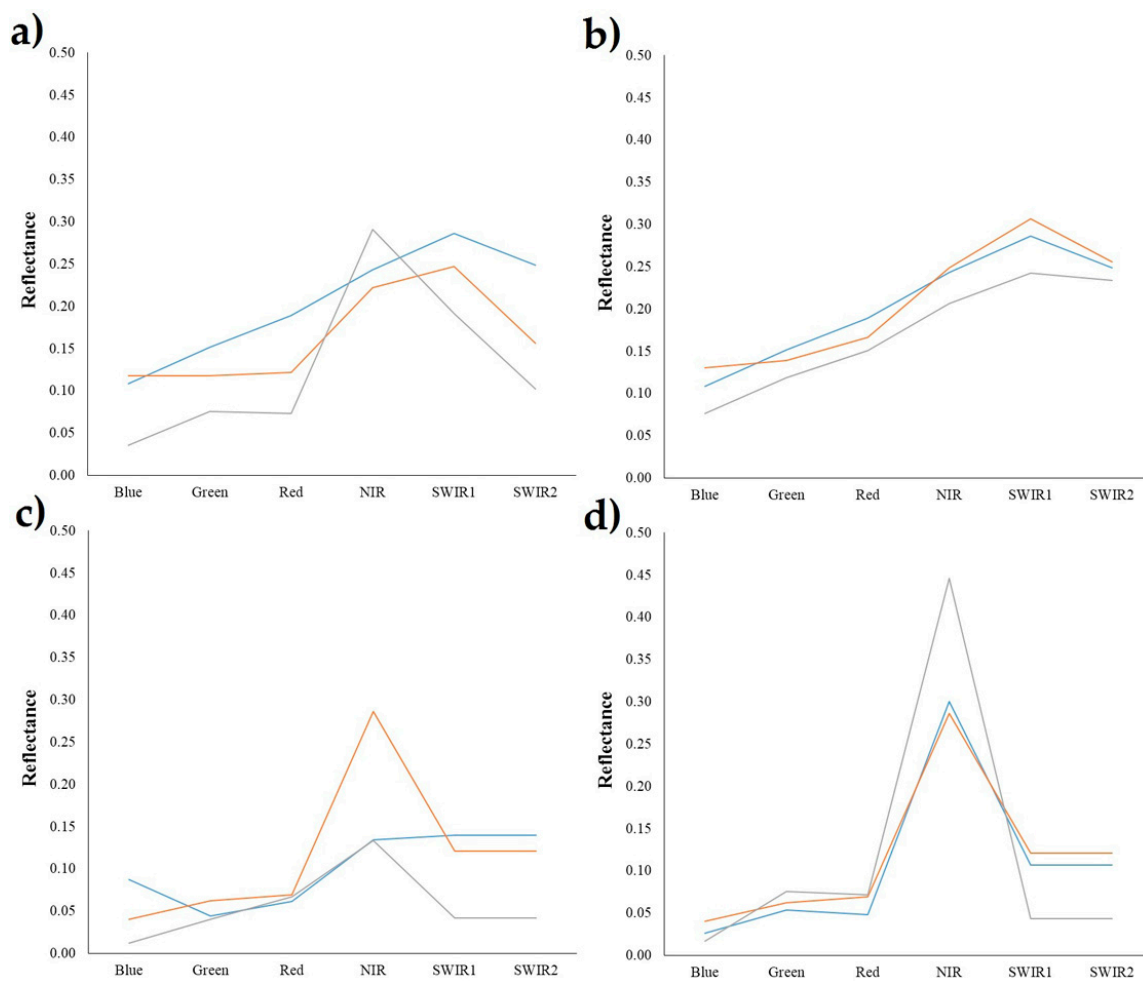


**Figure 6.** Spectral response of each correction method in Edén for 2010 (a); 2011 (b); 2013 (c); 2014 (d); ATCOR2 (—), DOS1 (—) and FLAASH (—). NIR: near infra-red; SWIR: shortwave infra-red.

The ANOVA applied to the data from the three PMS determined that there were significant differences ( $p < 0.05$ ) for all of the CMs in the visible region of the spectrum. The NIR showed a greater number of non-significant results for the three sites. In the case of Edén, all of the CMs showed significant differences for all of the bands, except for the SWIR 1 in 2011 (ATCOR2 and DOS1) and the red region in 2013 (DOS1 and FLAASH). Similarly, significant differences were also detected for El Sitio, with the exception of the NIR with the ATCOR2 method in 2010. Another two exceptions were the SWIR 1 in 2010 (ATCOR2) and the red region in 2013 (ATCOR2). Finally, the ANOVA detected significant differences for Teseachi; however, this site showed the greatest number of non-significant results.

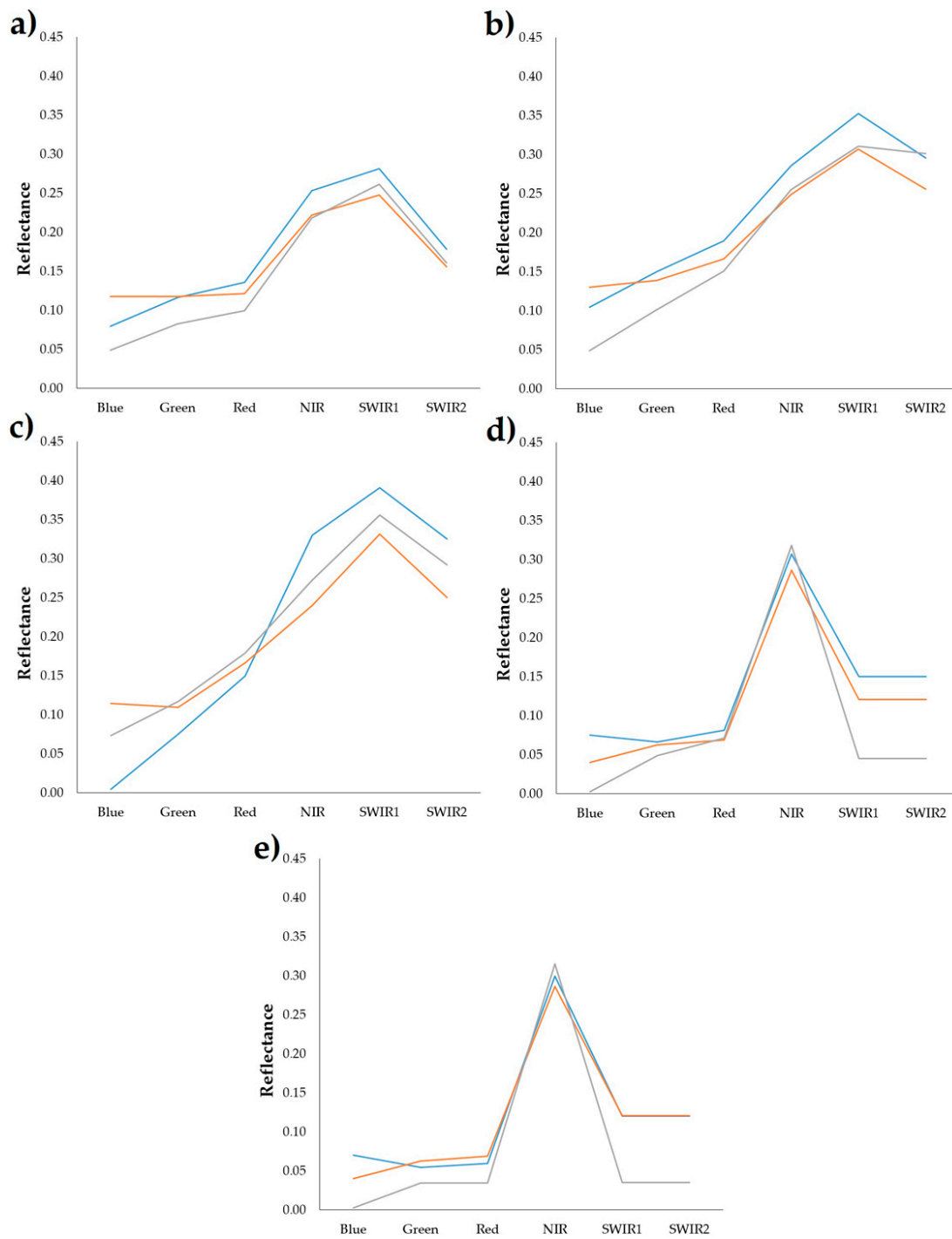


**Figure 7.** Spectral response of each correction method in El Sitio for 2010 (a); 2011 (b); 2012 (c); 2013 (d); 2014 (e); ATCOR2 (—), DOS1 (—), and FLAASH (—).

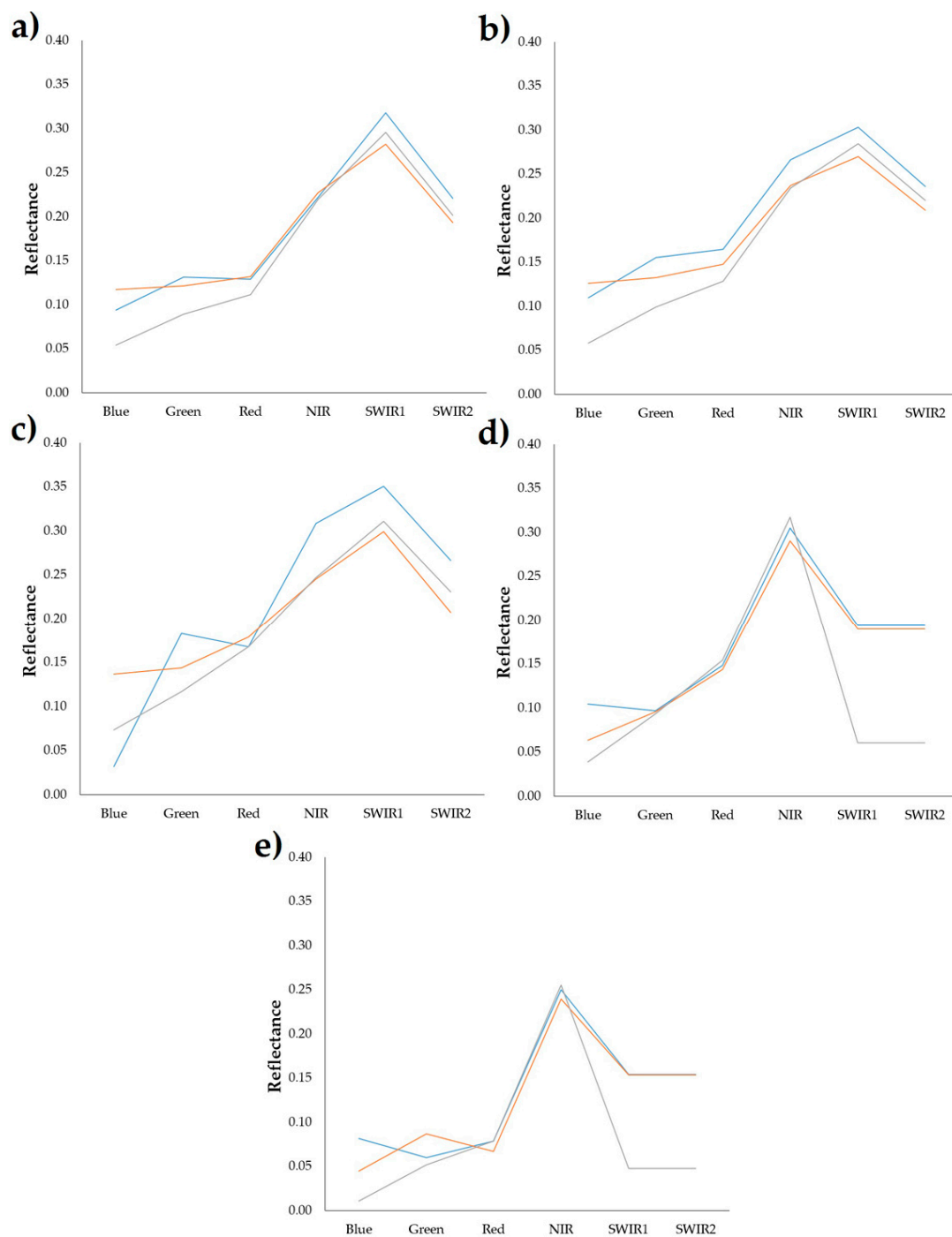


**Figure 8.** Spectral response of each correction method in Teseachi for 2010 (a); 2011 (b); 2012 (c); 2013 (d); 2014 (e); ATCOR2 (—), DOS1 (---), and FLAASH (—).

### 3.3. Estimated Annual Biomass

Table 2 shows the accuracy of the biomass estimation during 2010–2014 when applying the CMs to the scenes of each PMS. Variability on the values of  $R^2$  are observed among all the years and CMs. The contribution of the spectral bands to each SLR model was calculated. The results showed that, in Eden, the bands were not good biomass estimators ( $p > 0.05$ ) when used separately. For El Sitio, the results showed significant values of  $R^2$  ( $p < 0.05$ ) for the NIR in 2014 for the three CMs. In Teseachi, a larger number of significant values of  $R^2$  ( $p < 0.05$ ) were observed for the red region, NIR,

and SWIR 2. Finally, in Teseachi, the NIR and SWIR are the most relevant spectral regions for the prediction of biomass.

**Table 2.** Accuracy of the correction methods in the three permanent monitoring sites (PMS). The column of Band (spectrum region) corresponds to the spectral bands and the corresponding spectrum region that contributed the most for the biomass estimation.

No	Site	CA	Year	Band (Spectrum Region)	R <sup>2</sup>	RMSE (kg·ha <sup>-1</sup> )
1	Eden	ATCOR2	2010	1 (Blue)	0.35	72.01
2			2011	1 (Blue)	0.22	23.92
3			2012	n/d	n/d	n/d
4			2013	2 (Blue)	0.38	153.31
5			2014	6 (SWIR1)	0.05	321.27
6		DOS1	2010	2 (Green)	0.02	88.36
7			2011	1 (Blue)	0.12	25.42
8			2012	n/d	n/d	n/d
9			2013	5 (NIR)	0.19	174.70
10			2014	5 (NIR)	0.48 *	237.99
11		FLAASH	2010	1 (Blue)	0.19	80.11
12			2011	1 (Blue)	0.20	24.22
13			2012	n/d	n/d	n/d
14			2013	2 (Blue)	0.31	161.73
15			2014	7 (SWIR2)	0.04	323.04
1	El Sitio	ATCOR2	2010	1 (Blue)	0.08	98.32
2			2011	1 (Blue)	0.09	54.14
3			2012	2 (Green)	0.07	54.14
4			2013	2 (Blue)	0.40	34.43
5			2014	5 (NIR)	0.81 *	84.16
6		DOS1	2010	5 (SWIR1)	0.10	97.21
7			2011	7 (SWIR2)	0.26	302.29
8			2012	2 (Green)	0.07	59.06
9			2013	5 (NIR)	0.46 *	32.54
10			2014	5 (NIR)	0.81 *	84.16
11		FLAASH	2010	1 (Blue)	0.02	101.54
12			2011	1 (Blue)	0.27	29.10
13			2012	2 (Green)	0.08	58.94
14			2013	5 (NIR)	0.67 *	26.24
15			2014	5 (NIR)	0.79 *	86.66
1	Teseachi	ATCOR2	2010	5 (SWIR1)	0.26	82.58
2			2011	3 (Red)	0.40	52.92
3			2012	5 (SWIR1)	0.42	70.76
4			2013	7 (SWIR2)	0.76 *	48.79
5			2014	5 (NIR)	0.57 *	40.90
6		DOS1	2010	7 (SWIR2)	0.44 *	71.42
7			2011	3 (Red)	0.40	52.93
8			2012	7 (SWIR2)	0.72 *	48.65
9			2013	7 (SWIR2)	0.76 *	48.79
10			2014	5 (NIR)	0.42 *	40.90
11		FLAASH	2010	7 (SWIR2)	0.44 *	71.44
12			2011	3 (Red)	0.40	53.00
13			2012	7 (SWIR2)	0.72 *	60.76
14			2013	7 (SWIR2)	0.76 *	77.97
15			2014	6 (SWIR1)	0.57 *	40.61

\* = significant level ( $p < 0.05$ ), n/d = no data, CA = correction algorithm.

The results obtained could be related to the specific atmospheric parameters included as inputs in each of the models. The DOS1 method does not refer to the atmospheric profile [66] and FLAASH uses

global values for its atmospheric parameters [67]. Figures 9 and 10 show the variations of the values of  $R^2$  and RMSE obtained by the SLR analysis. The RMSE fluctuated in the three CMs, being DOS1 the one with the most stable and the lowest values.

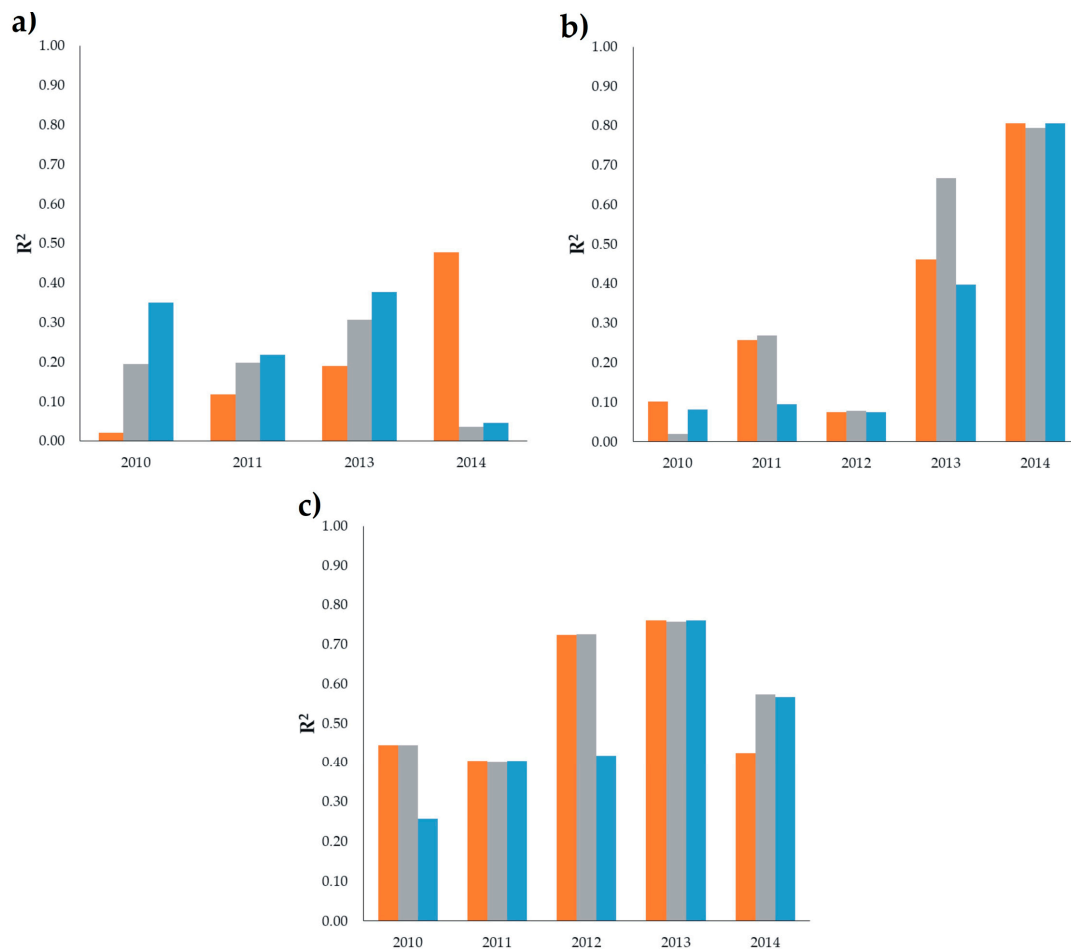


**Figure 9.** Variation in the precision of the correction methods represented by values of  $R^2$ . Eden (a); El Sitio (b); Teseachi (c); ATCOR2 (—), DOS1 (—) and FLAASH (—) through single band.

The results of the PC analysis for biomass estimation in the three PMS are shown in Table 3. Two main components were considered for the PC analysis, which represented at least 80% of the total data set variance. The analysis of the PCs served to group the spectral variance and to establish its relation to biomass production. Thus, each resulting component represents a reduced percentage of variability.

In the site Eden, the highest values of  $R^2$  were obtained for DOS1 when grouping the visible and the SWR1, as well as the SWIR2, regions. The FLAASH correction algorithm showed moderate values of  $R^2$  by grouping the visible region of the spectrum in PC1 and NIR, as well as SWIR in PC2. This result is in agreement with the findings by Hadjimitsis et al. [68] who obtained reliable PCs by grouping similar regions of the spectrum. The site El Sitio showed values of  $R^2$  greater than 0.71 and the components derived from DOS1 were the best biomass estimators. The rest of the methods did not obtain significant results. Teseachi showed values of  $R^2$  between 0.41 and 0.98. Table 3 shows the way the Spectral bands were grouped to form the principal components. Among the three CMs, DOS1 showed the most consistent outputs for all of the years.

Figures 11 and 12 show the variations of  $R^2$  and RMSE obtained by the SLR analysis between biomass and the spectral information. The site that showed the highest precision was El Sitio. The method of DOS1 produced the most stable and the most precise results among the sites.

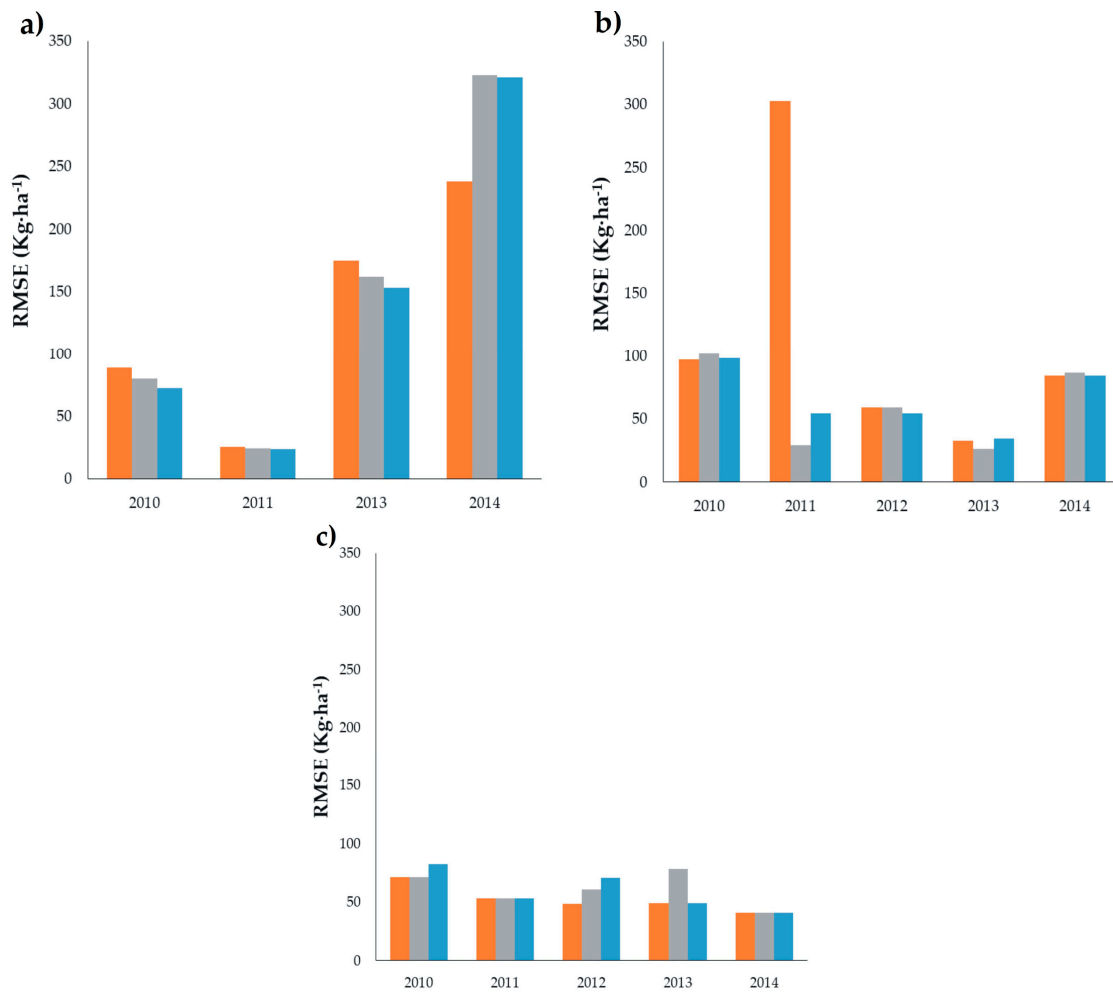


**Figure 10.** Variation in the precision of the correction methods represented by the RMSE ( $\text{kg}\cdot\text{ha}^{-1}$ ). Eden (a); El Sitio (b); Teseachi (c); ATCOR2 (—), DOS1 (—) and FLAASH (—) through single band.

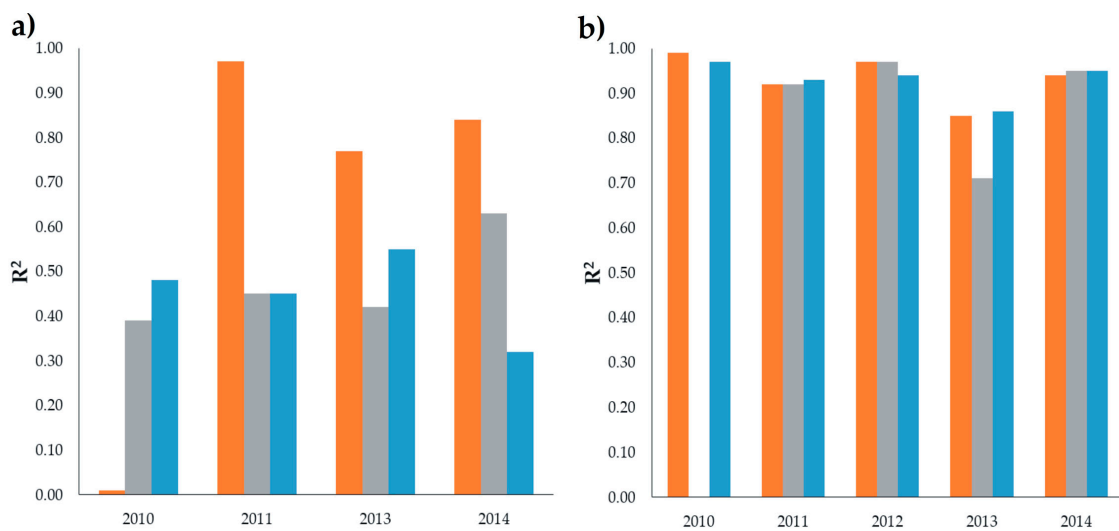


**Figure 11.** Cont.

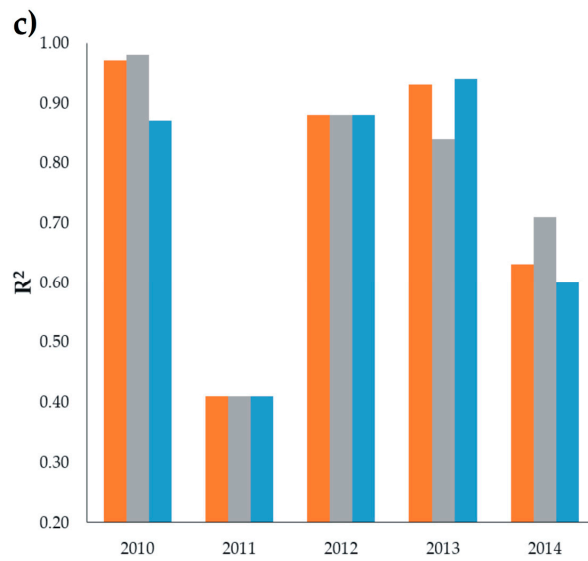


**Figure 11.** Variation in the precision of the correction methods represented by values of  $R^2$ . Eden (a); El Sitio (b); Teseachi (c); ATCOR2 (—), DOS1 (—), and FLAASH (—) through PC.

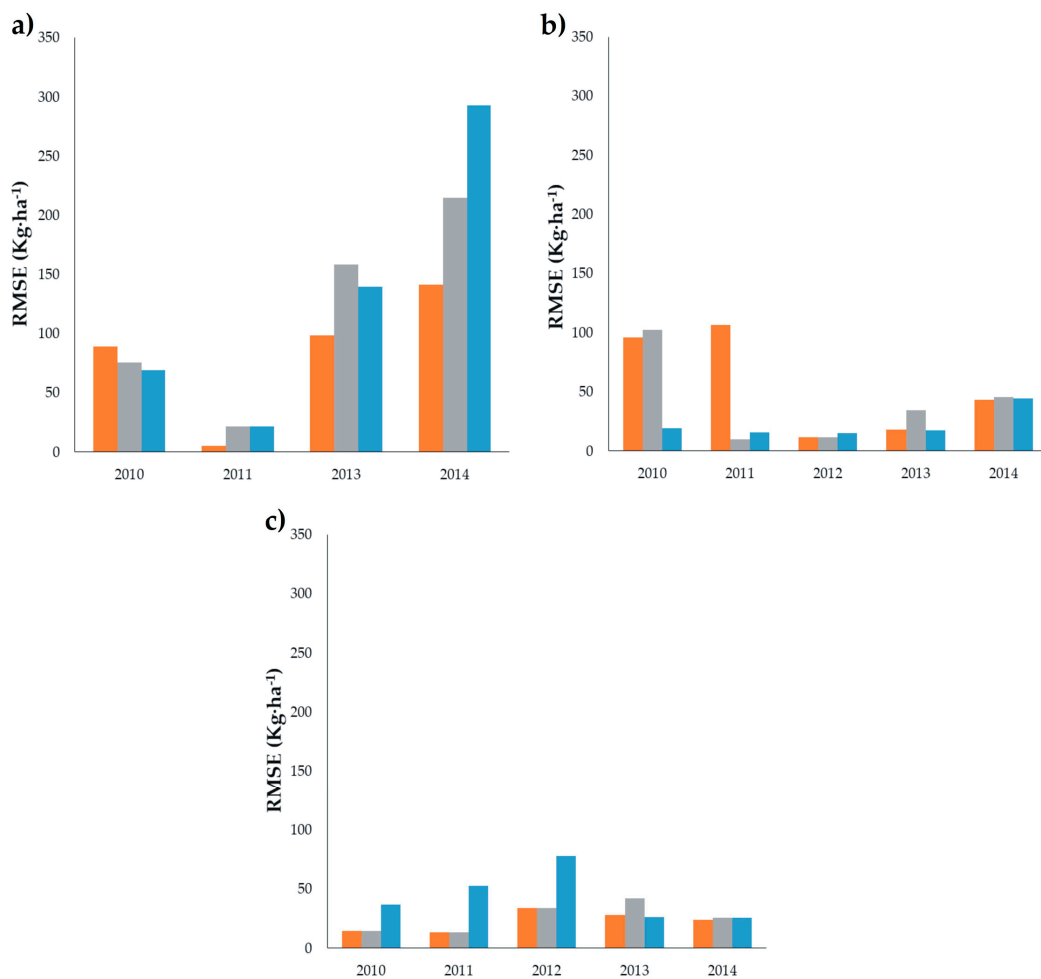


**Figure 12.** Variation in the precision of the correction methods represented by RMSE ( $\text{kg}\cdot\text{ha}^{-1}$ ). Eden (a); El Sitio (b); Teseachi (c); ATCOR2 (—), DOS1 (—), and FLAASH (—) through PC.

**Table 3.** Accuracy of the correction methods represented by the values of  $R^2$  and RMSE for biomass estimation in the three PMS and the spectral bands forming the principal components.

No	Site	Correction Method	Year	PC1	PC2	$R^2$	RMSE (kg·ha <sup>-1</sup> )
				Bands	Bands		
1			2010	1 2 3 4	5 7	0.48	69.08
2			2011	1 2 3	4 5 7	0.45	21.54
3		ATCOR2	2012	n/d	n/d	n/d	n/d
4			2013	2 3 4	6 7	0.55	139.53
5			2014	2 3 4	6 7	0.32	292.99
6	Eden		2010	1 2 3 4 5 7		0.01	88.78
7			2011	1 2	3 4 5 7	0.97 *	4.97
8		DOS1	2012	n/d	n/d	n/d	n/d
9			2013	2 3 4 6 7	5	0.77 *	98.49
10			2014	2 3 4 6 7	5	0.84 *	141.18
11			2010	1 4 7	3	0.39	75.30
12			2011	4 7	1 2 3	0.45	21.56
13		FLAASH	2012	n/d	n/d	n/d	n/d
14			2013	3 4 5 6 7	2	0.42	158.38
15			2014	2 3 4	5 6 7	0.63 *	214.41
16			2010	1 2 3	4 7	0.97 *	19.10
17			2011	1 2 3	4 5	0.93 *	15.82
18		ATCOR2	2012	2 3 4 5 7	1	0.94 *	15.20
19			2013	3 4 6 7	2 5	0.86 *	17.36
20			2014	2 3 4 6 7	5	0.95 *	44.52
21	El Sitio		2010	2 3 4 5 7		0.99 *	95.61
22			2011	1 2 3 4 5 7	7	0.92 *	106.37
23		DOS1	2012	2 3 4 5 7	1	0.97 **	11.46
24			2013	2 3 4 6 7	5	0.85 *	18.09
25			2014	2 3 4 6 7	5	0.94 *	43.24
26			2010	1 2 3 4 5 7		0.00	102.50
27			2011	2 3 4	1 5 7	0.92 *	9.90
28		FLAASH	2012	1 2	3 4 5 7	0.97 **	11.39
29			2013	3 4 6 7	2 5	0.71	34.29
30			2014	2 3 4 6 7	5	0.95 **	45.61
31			2010	1 2 3 4	5 7	0.87 *	36.92
32			2011	1 2 3		0.41	52.32
33		ATCOR2	2012	1 2 3 4	5 7	0.88 *	77.96
34			2013	3 4 5	2 6 7	0.94 *	25.92
35			2014	2 3 4 5 6 7		0.60 *	25.35
36	Teseachi		2010	1 2 3 4	5 7	0.97 **	14.69
37			2011	1 2 3		0.41	13.09
38		DOS1	2012	1 2 3 4	5 7	0.88 *	33.62
39			2013	2 3 6 7	4 5	0.93 *	28.03
40			2014	2 3 4 5 6 7		0.63 *	23.53
41			2010	1 2 3 4	5 7	0.98 **	14.63
42			2011	1 2 3		0.41	13.24
43		FLAASH	2012	1 2 3 4	5 7	0.88 *	33.49
44			2013	2 3 6 7	4 5	0.84 *	42.16
45			2014	2 6 7	3 4 5	0.71	25.50

\* = significant level at  $p < 0.05$ , \*\* = significant level at  $p < 0.01$ , n/d = no data.

The site Eden obtained low values of the coefficient of determination (0.3–0.5) when corrected with ATCOR2. By correcting the data with DOS1, the precision improved significantly ( $p < 0.05$ ) for the data of 2011–2014 with  $R^2$  values greater than 0.77. This indicates that DOS1 can estimate

biomass production with a greater precision in spite of the accelerated changes in the succession of the grassland and the great density, as well as diversity of plants, in the site.

El Sitio obtained precise results for biomass estimations by applying the three CMs, which indicates homogeneity in the reflectance of the grassland. For Teseachi, good yields were obtained in 2010, 2012, and 2013 with the three CMs, with a similar precision to El Sitio.

#### 4. Discussion

In this study, we have reviewed three correction methods of satellite images applied them to a temporal series of 12 scenes. The precision of each method was assessed through values of  $R^2$  and RMSE. The DOS1 method, which is the simplest, provided a reasonable correction in the bands of the visible spectrum [40,69]. Given that the input parameters for DOS1 are derived from the image itself, it makes the method relatively easy to implement. Thus, it is preferred over more sophisticated methods that require the acquisition of atmospheric or meteorological data [32,66,70]. The time required for each method can be a crucial factor when using multiple sets of images [71]. The methods of ATCOR2 and FLAASH required much more processing time than DOS1. These requirements limit their application, especially when the historical atmospheric information is limited [33,40,72]. The differences in the results from ATCOR2 and DOS1 were probably due to the availability of reliable atmospheric historical data, which may have conferred to DOS1 a better performance [33]. Likewise, the differences between ATCOR2 and FLAASH, when performing radiometric correction on spectral data from vegetation, may be due to the water content of such vegetation [73].

The CMs allowed for the conversion of digital numbers to reflectance values. The spectral reflectance of grasslands was low in the visible region for all of the three PMS during 2010–2014. Chlorophyll absorbs most of the light received on the photosynthetically active radiation range of the spectrum. Consequently, reflectance was higher in the NIR, SWIR 1, and SWIR 2, indicating a contrast between these and the aforementioned visible regions of the electromagnetic spectrum [74,75]. The variation in biomass production estimation for the period 2010–2014 can be largely explained by changes in vegetation, its growth conditions, and its distribution. As mentioned by Yan et al. [76], the growth conditions in semi-arid and arid regions are largely affected by temperature and precipitation. In addition, human activities, such as grazing and farming, importantly affect the vegetation distribution. It was observed that in the period when the scenes were taken, the spectral signature of the grassland varied along the years. This can be explained by the effects of density, weight, coverage, and shade, which are variable in grass communities [17,65].

The comparison of the different CMs was based on the bands or principal components that contributed the most to the estimations of biomass. This study proved that the DOS1 method may be enough for radiometric correction in grassland areas, given the data required, which include only a few parameters [73]. The results obtained in this study indicate that DOS1 is sufficient to correct images used in the estimation of structural variables of the grassland. In this sense, it may not be necessary to employ complex algorithms when evaluating areas of grassland [33,69].

The ANOVA applied to the three PMS revealed significant differences among DOS1, FLAASH, and ATCOR2 in the visible and the infra-red regions of the spectrum. This is consistent with the results reported by Vicente-Serrano et al. [48] and Nazeer et al. [45]. In general, band 4 showed the most non-significant differences, followed by bands 7 and 3.

The correlations between biomass production and the spectral data obtained the highest values when the bands of red and infra-red were employed. In contrast, the relationships between biomass and the spectral values of the visible region were weak, indicating the sensitivity of this spectral range to the atmospheric variation, which agrees with that reported by Roy and Ravan [77]. Thus, in the temporal estimation and quantification of biomass, the application of a method for radiometric correction is necessary to eliminate the temporal variability. For most of the studied years, we found that FLAASH showed the highest reflectance values in the NIR. Such high values affected the relationships between

biomass and spectral values. Previous studies have shown that high values of reflectance affect the estimations of biomass and the determination of potential areas for grassland production [69].

The low biomass production values predicted for the three PMS could be due to site conditions or the date of data collection. Thus, the evaluation period may not be the best period to estimate biomass by using multitemporal data from the Landsat sensor. Our results confirmed a lack of association between spectral and biomass data. The relationship between the biomass and the bands (Table 2), and between biomass and the principal components (Table 3), for all of the PMS evaluated confirmed that there was a high variability. Such variability could neither be explained by the spectral response of the bands nor by the principal components. It is possible that the high values of reflectance in the infra-red region that showed in the site Eden after applying the DOS1 method are due to the atmospheric dispersion [64].

For the atmospheric and radiometric corrections, we have documented the differences between the reflectance values after applying the CMs to the data from different sites. In comparison with other multitemporal studies [23,49,50], we have tested different CMs with a change of platform from Landsat 5 to Landsat 8 in grassland areas. In the site Eden, we found that the deviations between the estimated and measured biomass were high for 2013 and 2014. This happened when the biomass was estimated with both the SLR and the MLR. Thus, such deviations can be attributed to the change of platform (TM to OLI). This change can cause instability in the time series [78]. Eden was the site with the lowest values of the coefficient of determination. The MLR with PCs was performed to include all of the spectral variability and correlate it to biomass; however, the results showed low correlation values. Therefore, such spectral variability may be influenced by other sources of variation, such as climate, topography, and invasive species [9]. For El Sitio, and analyzing the data with SLR, low values of  $R^2$  were obtained; in contrast, higher correlations were found with the MLR. This shows that biomass can be greatly estimated from the spectral data. More precise estimates, evidenced with higher  $R^2$  values, were produced with the data from Teseachi when analyzed with both the SLR and the MLR. The correlation of biomass and spectral data determined through MLR showed that, in at least two of the three PMS, the variation can be explained with the set of bands of the visible and infra-red ranges of the spectrum. Conversely, in one of the sites, it is necessary to collect more variables to explain the biomass variation. The inclusion of PCs in the biomass estimation allowed for an explanation of the spectral variability more effectively.

## 5. Conclusions

Atmospheric correction is a crucial step in the pre-processing of satellite images. Landsat images and biomass data from the field were employed to test the precision of three algorithms of atmospheric correction. According to the results, DOS1 presented the highest correlation values, pointing it out as a good method for the atmospheric correction of Landsat images and its application for the estimation of grassland biomass production.

Determination of the grassland production for Teseachi obtained the lowest deviations between estimated and measured biomass when modelling this variable with both single and multiple linear regression. The precisions of the estimates were closely related to the temporal spectral stability of the images. For Eden, the results were the least precise, which indicates that there is a great variation in the terrain that is difficult to explain by the satellite images. Biomass estimation using field and spectral data, coupled with an adequate atmospheric correction method, can accurately reflect grassland characteristics. For future studies, models that consider the effects of climate, minimum and maximum temperatures, precipitation, and topographic data, such as elevation, slope, and aspect, could be tested for higher precisions.

Three correction methods have been proposed and tested in this study. The simplest algorithm, DOS1, provided a reasonable correction and estimated biomass accurately when employing bands in the visible and infra-red regions of the spectrum, at least for cloud-free scenes. Operationally, the DOS1 method, which derives its input parameters from the image itself and is relatively easy to implement,

may be more reliable to implement over more sophisticated methods, which require the acquisition of atmospheric or meteorological historical data.

In the multitemporal estimation of grassland biomass production employing spectral information, it is not necessary to apply complex radiometric correction procedures. The use of the DOS1 method provided good results given its nature of providing reliable results on dark surfaces. However, when the spectral signal is affected by various sources of variation, it may be necessary to apply high-precision radiometric corrections, such as ATCOR2 or FLAASH. To make continuous estimates of biomass by remote sensors, it is preferable to employ a set of homogeneous Landsat images provided by a single platform.

Precise estimates of biomass will allow for the quantification of potential carbon stores by grasslands, serve to regulate animal load based on temporal estimation, and ensure control on the use of the grassland biomass. Estimating the spatial distribution of biomass is of great importance to support the study of grassland ecology and its socioeconomic environment. This study proved that it is possible to estimate grassland biomass production by remote sensing through an SLR analysis. Grassland biomass maps can be used as a reference to assess the grassland condition, the grazing capacity, and potential animal production. The use of remote sensing tools in grassland ecosystems is important for their monitoring, conservation, and protection.

**Acknowledgments:** We deeply thank the Consejo Nacional de Ciencia y Tecnología (CONACYT-Mexico) for supporting the graduate studies of the first author of this manuscript.

**Author Contributions:** Jesús A. Prieto-Amparán and Alfredo Pinedo-Alvarez conceived and designed the research; Federico Villarreal-Guerrero and Eduardo Santellano-Estrada processed the data, analyzed it and elaborated the first draft; Martin Martinez-Salvador and Carlos Manjarrez-Domínguez substantially contributed to the editions and final revision of the present manuscript.

**Conflicts of Interest:** The authors declare no conflict of interest.

## References

1. Yang, Y.; Fang, J.; Pan, Y.; Ji, C. Aboveground biomass in Tibetan grasslands. *J. Arid Environ.* **2009**, *73*, 91–95. [[CrossRef](#)]
2. Jin, Y.X.; Yang, X.C.; Qiu, J.J.; Li, J.Y.; Gao, T.; Wu, Q.; Zhao, F.; Ma, H.L.; Yu, H.D.; Xu, B. Remote sensing-based biomass estimation and its spatio-temporal variations in temperate grassland, Northern China. *Remote Sens.* **2014**, *6*, 1496–1513. [[CrossRef](#)]
3. Craine, J.M. Long-term climate sensitivity of grazer performance: A cross-site study. *PLoS ONE* **2013**, *8*, e67065. [[CrossRef](#)] [[PubMed](#)]
4. Manjarrez-Domínguez, C.; Pinedo-Alvarez, A.; Pinedo-Alvarez, C.; Villarreal-Guerrero, F.; Cortes-Palacios, L. Vegetation landscape analysis due to land use changes on arid lands. *Pol. J. Ecol.* **2015**, *63*, 272–279. [[CrossRef](#)]
5. Estrada-Castillón, E.; Scott-Morales, L.; Villarreal-Quintanilla, J.A.; Jurado-Ybarra, E.; Cotera-Correa, M.; Cantú-Ayala, C.; García-Pérez, J. Clasificación de los pastizales halófilos del noreste de México asociados con perrito de las praderas (*Cynomys mexicanus*): Diversidad y endemismo de especies. *Revista Mexicana de Biodiversidad* **2010**, *81*, 401–416.
6. He, C.; Zhang, Q.; Li, Y.; Li, X.; Shi, P. Zoning grassland protection area using remote sensing and cellular automata modeling—A case study in Xilingol steppe grassland in northern China. *J. Arid Environ.* **2005**, *63*, 814–826. [[CrossRef](#)]
7. Fan, J.W.; Zhong, H.P.; Harris, W.; Yu, G.R.; Wang, S.Q.; Hu, Z.M.; Yue, Y.Z. Carbon storage in the grassland of China based on field measurement of above- and below- ground biomass. *Clim. Chang.* **2007**, *86*, 375–396. [[CrossRef](#)]
8. Ruppert, J.C.; Linstädter, A. Convergence between ANPP estimation methods in grasslands—A practical solution to the comparability dilemma. *Ecol. Indic.* **2014**, *36*, 524–531. [[CrossRef](#)]
9. Xie, Y.C.; Sha, Z.Y.; Yu, M.; Bai, Y.F.; Zhang, L. A comparison of two models with Landsat data for estimating above ground grassland biomass in Inner Mongolia, China. *Ecol. Model.* **2009**, *220*, 1810–1818. [[CrossRef](#)]

10. Goetz, S.J.; Prince, S.D.; Goward, S.N.; Thawley, M.M.; Small, J. Satellite remote sensing of primary production: An improved production efficiency modeling approach. *Ecol. Model.* **1999**, *122*, 239–255. [[CrossRef](#)]
11. Li, J.Y.; Yang, X.C.; Jin, Y.X.; Yang, Z.; Huang, W.G.; Zhao, L.N.; Gao, T.; Yu, H.D.; Ma, H.L.; Qin, Z.H.; et al. Monitoring and analysis of grassland desertification dynamics using Landsat images in Ningxia, China. *Remote Sens. Environ.* **2003**, *138*, 19–26. [[CrossRef](#)]
12. Zhao, P.; Dengsheng, L.; Guangxing, W.; Chuping, W.; Yujie, H.; Shuquan, Y. Examining spectral reflectance saturation in Landsat imagery and corresponding solutions to improve forest aboveground biomass estimation. *Remote Sens.* **2016**, *8*, 469. [[CrossRef](#)]
13. Naesset, E.; Gobakken, T.; Bollandsås, O.M.; Gregoire, T.G.; Nelson, R.; Ståhl, G. Comparison of precision of biomass estimates in regional field sample surveys and airborne LiDAR-assisted surveys in Hedmark County, Norway. *Remote Sens. Environ.* **2013**, *130*, 108–120. [[CrossRef](#)]
14. Schino, G.; Borfecchia, F.; De Cecco, L. Satellite estimate of grass biomass in a mountainous range in central Italy. *Agrofor. Syst.* **2003**, *59*, 157–162. [[CrossRef](#)]
15. Marsett, C.R.; Qi, J.; Heilman, P.; Biedenbender, H.S.; Watson, C.M.; Amer, S.; Weltz, M.; Goodrich, D.; Marsett, R. Remote sensing for grassland management in the arid Southwest. *Rangel. Ecol. Manag.* **2006**, *59*, 530–540. [[CrossRef](#)]
16. Dusseux, P.; Huber-Moy, L.; Corpetti, T.; Vertès, F. Evaluation of SPOT imagery for the estimation of grassland biomass. *Int. J. Appl. Earth Obs.* **2015**, *38*, 72–77. [[CrossRef](#)]
17. Rodríguez-Maturino, A.; Martínez-Guerrero, J.H.; Chairez-Hernández, I.; Pereda-Solis, M.E.; Villarreal-Guerrero, F.; Renteria-Villalobos, M.; Pinedo-Alvarez, A. Mapping land cover and estimating the grassland structure in a priority area of the Chihuahuan desert. *Land* **2017**, *6*, 70. [[CrossRef](#)]
18. Cohen, W.B.; Goward, S.N. Landsat's role in ecological applications of remote sensing. *BioScience* **2004**, *54*, 535–545. [[CrossRef](#)]
19. Woodcock, C.E.; Macomber, S.A.; Pax-Lenney, M.; Cohen, W.C. Monitoring large areas for forest change using Landsat: Generalization across space, time and Landsat sensors. *Remote Sens. Environ.* **2001**, *78*, 194–203. [[CrossRef](#)]
20. Wulder, M.A.; White, J.C.; Goward, S.N.; Masek, J.G.; Irons, J.R.; Herold, M.; Cohen, W.B.; Loveland, T.R.; Woodcock, C.E. Landsat continuity: Issues and opportunities for land cover monitoring. *Remote Sens. Environ.* **2008**, *112*, 955–969. [[CrossRef](#)]
21. Hansen, M.C.; Loveland, T.R. A review of large are monitoring of land cover change using Landsat data. *Remote Sens. Environ.* **2012**, *122*, 66–74. [[CrossRef](#)]
22. Chander, G.; Markham, B.L.; Helder, D.L. Summary of current radiometric calibration coefficients for Landsat MSS, TM, ETM+, and EO-1 ALI sensors. *Remote Sens. Environ.* **2009**, *113*, 893–903. [[CrossRef](#)]
23. Tan, K.C.; San Lim, H.; Matjafri, M.Z.; Abdullah, K. A comparison of radiometric correction techniques in the evaluation of the relationship between LST and NDVI in Landsat imagery. *Environ. Monit. Assess.* **2012**, *184*, 3813–3829. [[CrossRef](#)] [[PubMed](#)]
24. Roy, D.P.; Zhang, H.K.; Ju, J.; Gomez-Dans, J.L.; Lewis, P.E.; Schaaf, C.B.; Sun, Q.; Li, J.; Hung, H.; Kovalskyy, V. A general method to normalized Landsat reflectance data to nadir BRDF adjusted reflectance. *Remote Sens. Environ.* **2016**, *176*, 255–271. [[CrossRef](#)]
25. Körner, I.; Oreopoulos, L.; Feingold, G.; Remer, L.A.; Altaratz, O. How small is a small cloud? *Atmos. Chem. Phys.* **2008**, *8*, 3855–3864. [[CrossRef](#)]
26. Zelazowski, P.; Sayer, A.M.; Thomas, G.E.; Grainger, R.G. Reconciling satellite-derived atmospheric properties with fine-resolution land imagery: Insights for atmospheric correction. *J. Geophys. Res. Atmos.* **2011**, *116*. [[CrossRef](#)]
27. Pons, X.; Pesquer, L.; Cristóbal, J.; González-Guerrero, O. Automatic and improved radiometric correction of Landsat imagery using reference values from MODIS surface reflectance images. *Int. J. Appl. Earth. Obs.* **2014**, *33*, 243–254. [[CrossRef](#)]
28. Pinedo, A.C.; Pinedo, A.A.; Martinez, Q.R.M. Análisis de áreas deforestadas en la región centro-norte de la Sierra Madre Occidental, Chihuahua, México. *Tecnociencia Chihuahua*. **2007**, *1*, 36–43.
29. Vázquez-Quintero, G.; Solís-Moreno, R.; Pompa-García, M.; Villarreal-Guerrero, F.; Pinedo-Alvarez, C.; Pinedo-Alvarez, A. Detection and projection of forest changes by using the Markov Chain Model and Cellular Automata. *Sustainability* **2016**, *8*, 236. [[CrossRef](#)]

30. Prieto-Amparán, J.A.; Pinedo-Alvarez, A.; Villarreal-Guerrero, F.; Pinedo-Alvarez, C.; Morales-Nieto, C.; Manjarrez-Domínguez, C. Past and future spatial growth dynamics of Chihuahua city, Mexico: Pressures for land use. *ISPRS Int. Geo-Inf.* **2016**, *5*, 235. [[CrossRef](#)]
31. Chavez, P.S., Jr. An improved dark-object subtraction technique for atmospheric scattering correction of multispectral data. *Remote Sens. Environ.* **1988**, *24*, 459–479. [[CrossRef](#)]
32. Kaufman, Y.J.; Wald, A.E.; Remer, L.A.; Gao, B.C.; Li, R.-R.; Flynn, L. The MODIS 2.1- $\mu$ m channel-correlation with visible reflectance for use in remote sensing of aerosol. *IEEE Trans. Geosci. Remote Sens.* **1997**, *35*, 1286–1298. [[CrossRef](#)]
33. Janzen, T.D.; Fredeen, L.A.; Wheate, D.R. Radiometric correction techniques and accuracy assessment for Landsat TM data in remote forested regions. *Can. J. Remote Sens.* **2006**, *32*, 330–340. [[CrossRef](#)]
34. Lyapustin, A.; Williams, D.L.; Markham, B.; Irons, J.; Holben, B.; Wang, Y. A method for unbiased high-resolution aerosol retrieval from Landsat. *J. Atmos. Sci.* **2004**, *61*, 1233–1244. [[CrossRef](#)]
35. Richter, R.; Schlapfer, D.; Muller, A. An automatic atmospheric correction algorithm for visible/NIR imagery. *Int. J. Remote Sens.* **2006**, *27*, 2077–2085. [[CrossRef](#)]
36. Kruse, F.A. Comparison of ATREM, ACORN, and FLAASH atmospheric corrections using low-altitude AVIRIS data of Boulder, CO. In Proceedings of the 13th JPL Airborne Geoscience Workshop, Pasadena, CA, USA, 31 March–2 April 2004.
37. Neubert, M.; Meinel, G. Atmospheric and terrain correction of IKONOS imagery using ATCOR3. In Proceedings of the ISPRS Workshop 2005: High-Resolution Earth Imaging for Geospatial Information, Hannover, Germany, 17–20 May 2005.
38. Geosystems. *Haze Reduction, Atmospheric and Topographic Correction. User Manual ATCOR2 and ATCOR3*; Geosystems GmbH: Geneva, Switzerland, 2013.
39. Paolini, L.; Grings, F.; Sobrino, J.A.; Jiménez Muñoz, J.C.; Karszenbaum, H. Radiometric correction effects in Landsat multi-date/multi-sensor change detection studies. *Int. J. Remote Sens.* **2006**, *27*, 685–704. [[CrossRef](#)]
40. Cui, Q.Y.; Gaillard, M.J.; Lemdahl, G.; Stenberg, L.; Sugita, S.; Zernova, G. Historical land-use and landscape change in Southern Sweden and implications for present and future biodiversity. *Ecol. Evol.* **2014**, *4*, 3555–3570. [[CrossRef](#)] [[PubMed](#)]
41. El Hajj, M.; Bégué, A.; Lafrance, B.; Hagolle, O.; Dedieu, G.; Rumeau, M. Relative radiometric normalization and atmospheric correction of a SPOT 5 time series. *Sensors* **2008**, *8*, 2774–2791. [[CrossRef](#)] [[PubMed](#)]
42. Chang, J.; Clay, D.E.; Leigh, L.; Aaron, D.; Dalsted, K.; Volz, M. Evaluating modified atmospheric correction methods for Landsat Imagery: Image-based and model-based calibration methods. *Commun. Soil Sci. Plan.* **2008**, *39*, 1532–1545. [[CrossRef](#)]
43. Callieco, F.; Dell’Acqua, F. A comparison between two radiative transfer models for atmospheric correction over a wide range of wavelengths. *Int. J. Remote Sens.* **2011**, *32*, 1357–1370. [[CrossRef](#)]
44. Agrawal, G.; Sarup, J.; Bhopal, M. Comparison of QUAC and FLAASH atmospheric correction modules on EO-1 Hyperion data of Sanchi. *Int. J. Adv. Eng. Sci. Technol.* **2011**, *4*, 178–186.
45. Nazeer, M.; Nichol, J.E.; Yung, Y.K. Evaluation of atmospheric correction models and Landsat surface reflectance product in an urban coastal environment. *Int. J. Remote Sens.* **2014**, *35*, 6271–6291. [[CrossRef](#)]
46. López-Serrano, P.M.; Corral-Rivas, J.J.; Díaz-Varela, R.A.; Álvarez-González, J.G.; López-Sánchez, C.A. Evaluation of radiometric and atmospheric correction algorithms for aboveground forest biomass estimation using Landsat 5 TM data. *Remote Sens.* **2016**, *8*, 369. [[CrossRef](#)]
47. Martins, V.S.; Barbosa, C.C.F.; de Carvalho, L.A.S.; Jorge, D.S.F.; Lobo, F.D.L.; Novo, E.M.L.D.M. Assessment of atmospheric correction methods for Sentinel-2 MSI images applied to Amazon floodplain lakes. *Remote Sens.* **2017**, *9*, 322. [[CrossRef](#)]
48. Vicente-Serrano, S.M.; Pérez-Cabello, F.; Lasanta, T. Assessment of radiometric correction techniques in analyzing vegetation variability and change using time series of Landsat images. *Remote Sens. Environ.* **2008**, *112*, 3916–3934. [[CrossRef](#)]
49. Nguyen, H.C.; Jung, J.; Lee, J.; Choi, S.U.; Hong, S.Y.; Heo, J. Optimal atmospheric correction for above-ground forest biomass estimation with the ETM+ remote sensor. *Sensors* **2015**, *15*, 18865–18886. [[CrossRef](#)] [[PubMed](#)]
50. Raab, C.; Barrett, B.; Cawkwell, F.; Green, S. Evaluation of multi-temporal and multi-sensor atmospheric correction strategies for land-cover accounting and monitoring in Ireland. *Remote Sens. Lett.* **2015**, *6*, 784–793. [[CrossRef](#)]

51. CCG-SAGARPA; COLPOS. *Manual de Campo Para la Red Básica del Sistema Nacional de Monitoreo Terrestre Orientado a la Ganadería*; Coordinación General de Ganadería de la Secretaría de Agricultura, Ganadería, Desarrollo Rural, Pesca y Alimentación: Distrito Federal, Mexico, 2009.
52. CONABIO (Comisión Nacional para el Conocimiento y Uso de la Biodiversidad). *La Biodiversidad en Chihuahua: Estudio de Estado*; Comisión Nacional para el Conocimiento y Uso de la Biodiversidad: Distrito Federal, Mexico, 2014.
53. Jurado, G.P.; Saucedo, T.R.A.; Morales, N.C.R.; Martínez, S.M. *Almacén y Captura de Carbono en Pastizales y Matorrales de Chihuahua*; INIFAP: Chihuahua, Mexico, 2013.
54. Samson, F.B.; Knopf, F.L.; Ostlie, W.R. Great Plains ecosystems: Past, present, and future. *Wildl. Soc. Bull.* **2004**, *32*, 6–15. [[CrossRef](#)]
55. IUCN (International Union for Conservation of Nature). Available online: <http://www.iucnredlist.org/details/18868/0> (accessed on 20 November 2016).
56. Ni, J. Estimating net primary productivity of grasslands from field biomass measurements in temperate northern China. *Plant Ecol.* **2004**, *174*, 217–234. [[CrossRef](#)]
57. United States Geological Survey. Available online: <http://glovis.usgs.gov> (accessed on 20 June 2016).
58. Barsi, J.A.; Lee, K.; Kvaran, G.; Markham, B.L.; Pedelty, J.A. The spectral response of the Landsat-8 operational land imager. *Remote Sens.* **2014**, *6*, 10232–10251. [[CrossRef](#)]
59. Berk, A.; Bernstein, L.S.; Anderson, G.P.; Acharya, P.K.; Robertson, D.C.; Chetwynd, J.H.; Adler-Golden, S.M. MODTRAN cloud and multiple scattering upgrades with application to AVIRIS. *Remote Sens. Environ.* **1998**, *65*, 367–375. [[CrossRef](#)]
60. Marcello, J.; Eugenio, F.; Perdomo, U.; Medina, A. Assessment of atmospheric algorithms to retrieve vegetation in natural protected areas using multispectral high resolution imagery. *Sensors* **2016**, *16*, 1624. [[CrossRef](#)] [[PubMed](#)]
61. Adler-Golden, S.; Berk, A.; Bernstein, L.S.; Richtsmeier, S.; Acharya, P.K.; Matthew, M.W.; Chetwynd, J.H. FLAASH, A MODTRAN4 atmospheric correction package for hyperspectral data retrievals and simulations. In Proceedings of the 7th Annual JPL Airborne Earth Science Workshop, Pasadena, CA, USA, 4–8 March 1998; pp. 9–14.
62. Anderson, G.P.; Felde, G.W.; Hoke, M.L.; Ratkowski, A.J.; Cooley, T.W.; Chetwynd, J.H.; Bernstein, L.S. MODTRAN4-based atmospheric correction algorithm: FLAASH (Fast Line-of-sight Atmospheric Analysis of Spectral Hypercubes). In *Algorithms and Technologies for Multispectral, Hyperspectral, and Ultraspectral Imagery VIII*; Society of Photo Optics: Orlando, FL, USA, 2002; Volume 4725, pp. 65–72.
63. Congedo, L. *Semi-Automatic Classification Plugin for QGIS*; Technical Report; Sapienza University, ACC Dar Project: Rome, Italy, 2013.
64. Lu, D.; Mausel, P.; Brondizio, E.; Moran, E. Assessment of atmospheric correction methods for Landsat TM data applicable to Amazon basin LBA research. *Int. J. Remote Sens.* **2002**, *23*, 2651–2671. [[CrossRef](#)]
65. Manakos, I.; Manevski, K.; Kalaitzidis, C.; Edler, D. Comparison between atmospheric correction modules on the basis of Worldview-2 imagery and in situ spectroradiometric measurements. In Proceedings of the 7th EARSeL Workshop on Imaging Spectroscopy, Edinburgh, UK, 11–13 April 2011; pp. 1–12.
66. Chavez, P.S. Image-based atmospheric corrections revisited and improved. *Photogramm. Eng. Remote Sens.* **1996**, *62*, 1025–1036.
67. Matthew, M.W.; Adler-Golden, S.M.; Berk, A.; Richtsmeier, S.C.; Levine, R.Y.; Bernstein, L.S.; Acharya, P.K.; Anderson, G.P.; Felde, G.W.; Hoke, M.P. Status of atmospheric correction using a MODTRAN4-based algorithm. In Proceedings of the Algorithms for Multispectral, Hyperspectral, and Ultraspectral Imagery VI, Orlando, FL, USA, 24–26 April 2000; pp. 199–207.
68. Hadjimitsis, D.G.; Clayton, C.R.I.; Hope, V.S. An assessment of the effectiveness of atmospheric correction algorithms through the remote sensing of some reservoirs. *Int. J. Remote Sens.* **2004**, *25*, 3651–3674. [[CrossRef](#)]
69. Song, C.; Woodcock, C.E.; Seto, K.C.; Lenney, M.P.; Macomber, S.A. Classification and change detection using Landsat TM data: When and how to correct atmospheric effects? *Remote Sens. Environ.* **2001**, *75*, 230–244. [[CrossRef](#)]
70. Liang, S.; Fang, H.; Morisette, J.T.; Chen, M.; Shuey, C.J.; Walthall, C.L.; Daughtry, C.S. Atmospheric correction of Landsat ETM+ land surface imagery. II. Validation and applications. *IEEE Trans. Geosci. Remote Sens.* **2002**, *40*, 2736–2746. [[CrossRef](#)]

71. Mahiny, A.S.; Turner, B.J. A comparison of four common atmospheric correction methods. *Photogramm. Eng. Remote Sens.* **2007**, *73*, 361–368. [[CrossRef](#)]
72. Mason, S.; Kruczkiewicz, A.; Ceccato, P.; Crawford, A. *Accessing and Using Climate Data and Information in Fragile, Data-Poor States*; International Institute for Sustainable Development: Winnipeg, MB, Canada, 2015.
73. Wu, J.; Wang, D.; Bauer, M.E. Image-based atmospheric correction of QuickBird imagery of Minnesota cropland. *Remote Sens. Environ.* **2005**, *99*, 315–325. [[CrossRef](#)]
74. Chuvieco, E.; Aguado, I.; Yebra, M.; Nieto, H.; Salas, J.; Pilar, M.M.; Vilar, L.; Martínez, J.; Martín, S.; Ibarra, P.; et al. Development of a framework for fire risk assessment using remote sensing and geographic information system technologies. *Ecol. Model.* **2010**, *221*, 46–58. [[CrossRef](#)]
75. Sonobe, R.; Yamaya, Y.; Tani, H.; Wang, X.; Kobayashi, N.; Mochizuki, K. Mapping crop cover using multi-temporal Landsat 8 OLI imagery. *Int. J. Remote Sens.* **2017**, *38*, 4348–4361. [[CrossRef](#)]
76. Yan, J.; Zhu, C.; Liu, W.; Luo, F.; Mi, J.; Ren, Y.; Li, J.; Sang, T. High photosynthetic rate and water use efficiency of *Miscanthus lutarioriparius* characterize an energy crop in the semiarid temperate region. *GCB Bioenergy* **2015**, *7*, 207–218. [[CrossRef](#)]
77. Roy, P.S.; Ravan, S.A. Biomass estimation using satellite remote sensing data—An investigation on possible approaches for natural forest. *J. Biosci.* **1996**, *21*, 535–561. [[CrossRef](#)]
78. Schroeder, T.A.; Cohen, W.B.; Song, C.; Canty, M.J.; Yang, Z. Radiometric correction of multi-temporal Landsat data for characterization of early successional forest patterns in western Oregon. *Remote Sens. Environ.* **2006**, *103*, 16–26. [[CrossRef](#)]



© 2018 by the authors. Licensee MDPI, Basel, Switzerland. This article is an open access article distributed under the terms and conditions of the Creative Commons Attribution (CC BY) license (<http://creativecommons.org/licenses/by/4.0/>).